European Cells and Materials Vol.52 2025 (pages 98–113) DOI: 10.22203/eCM.v052a07 ISSN 1473-2262

Original Article

SEAWATER-CONTAMINATED ULNAR RABBIT BONE DEFECTS REPAIR USING 3D-PRINTED β-TCP/VANCOMYCIN COMPOSITE SCAFFOLDS

H.D. Lao[1,§], D. Liu[2,§], R. Yi[3], Y.N. Yuan[1], M. Zhao[4], G.S. Li[1], X.Y. Nie[1], J.L. Gu[1], X.M. Cai[1], H. Li[1], S.E. Lin[5,6,7,]* and J.J. Zhou[1,]*

[1] Department of Orthopaedics, 908th Hospital of Chinese People's Liberation Army Joint Logistics Support Force (The Great Wall affiliated Hospital, Jiangxi Medical College, Nanchang University), 330001 Nanchang, Jiangxi, China
[2] Department of Orthopaedics, General Hospital of Chinese People's Liberation Army Western Theater Command, 610038 Chengdu, Sichuan, China
[3] Department of Orthopaedics, 7th Medical Centre, Chinese PLA General Hospital, 100700 Beijing, China
[4] Department of Orthopaedics, YingTan People's Hospital, 335000 Yingtan, Jiangxi, China
[5] Stem Cells and Regenerative Medicine Laboratory, Li Ka Shing Institute of Health Sciences, The Chinese University of Hong Kong, Prince of Wales Hospital, 999077 Shatin, Hong Kong, China
[6] Department of Orthopaedics & Traumatology, Musculoskeletal Research Laboratory, Faculty of Medicine, The Chinese University of Hong Kong, Prince of Wales Hospital, 999077 Shatin, Hong Kong, China
[7] Orthopaedic Center, The Affiliated Hospital of Guangdong Medical University, Guangdong Medical University, 524001 Zhanjiang, Guangdong, China
[§] These authors contributed equally.

Abstract

Background: Repairing extensive bone defects following seawater immersion poses a significant challenge for orthopedic surgeons. Recent advancements in three-dimensional (3D) printing technology have demonstrated considerable potential in fabricating scaffolds with optimized morphological structures and superior biological properties. However, the specific characteristics and therapeutic efficacy of 3D-printed nano beta-tricalcium phosphate (β-TCP) scaffolds in the repair of seawater-immersed rabbit ulna bone defects remain inadequately explored. **Methods**: Nano-β-TCP scaffolds were fabricated via stereo lithography apparatus (SLA) and characterized using scanning electron microscope (SEM), X-ray diffraction, and mechanical testing. Vancomycin-loaded scaffolds were implanted in 18 rats, with drug release profiles monitored over a 56-day period. Thirty-six rabbits were assigned to three groups to assess scaffold performance in 1.5 cm seawater-immersed ulnar defects. Serum tumor necrosis factor-alpha (TNF-α) levels were measured pre- and post-implantation to evaluate inflammatory responses. Bone repair was assessed through X-ray, histological analysis, and micro-computed tomography (micro-CT) scanning. *In vitro* antibacterial efficacy was also evaluated. **Results**: The scaffold exhibited a cylindrical porous structure with dimensions of 0.5 cm in both diameter and height. The average pore size was approximately 400 μm, with a porosity of 53 %, and a compressive strength of 170 N. The scaffold demonstrated sustained vancomycin release over 56 days. *In vivo*, implantation of the scaffolds resulted in a significant reduction in serum TNF-α levels ($p < 0.05$) and promoted new bone formation compared to controls ($p < 0.05$). Histological and micro-CT analyses confirmed superior bone repair, with increased expression of osteocalcin (OCN), osteopontin (OPN), and vascular endothelial growth factor (VEGF). The scaffolds exhibited robust antibacterial activity after 72 hours. **Conclusions**: 3D-printed nano-β-TCP scaffolds offer an effective solution for repairing seawater-immersed bone defects and significantly enhance bone regeneration.

Keywords: Materials science, biomedical materials, orthopedics, nanomaterials.

***Address for correspondence**: S.E. Lin, Stem Cells and Regenerative Medicine Laboratory, Li Ka Shing Institute of Health Sciences, The Chinese University of Hong Kong, Prince of Wales Hospital, 999077 Shatin, Hong Kong, China; Department of Orthopaedics & Traumatology, Musculoskeletal Research Laboratory, Faculty of Medicine, The Chinese University of Hong Kong, Prince of Wales Hospital, 999077 Shatin, Hong Kong, China. Email: Sienlin@cuhk.edu.hk; J.J. Zhou, Department of Orthopaedics, 908th Hospital of Chinese People's Liberation Army Joint Logistics Support Force (The Great Wall affiliated Hospital, Jiangxi Medical College, Nanchang University), 330001 Nanchang, Jiangxi, China. Email: Zjjortho@163.com.

Introduction

Bone defect repair presents a persistent challenge in orthopedics [1,2]. Defects arising from various causes often fail to heal autonomously, potentially resulting in nonunion and functional impairments that severely diminish patients' quality of life [3,4]. As naval military capabilities continue to evolve globally, the frequency of seawater-contaminated wounds sustained during naval warfare has risen, thereby increasing the demand for effective treatment approaches [5,6]. Among these injuries, bone damage is a common consequence of trauma. Due to the distinct characteristics of the maritime environment, individuals injured at sea frequently experience open wounds with prolonged seawater immersion. The hyperosmolarity, alkalinity, and microbial contamination of seawater contribute to multiple adverse effects on injured tissues, including osmotic fluid shifts, impaired microcirculation, tissue ischemia and hypoxia, and an elevated risk of infection. These factors collectively complicate the repair of open wounds and bone defects, substantially heightening the risk of disability and compromising patient quality of life [7,8]. This issue demands urgent attention from medical teams involved in naval combat rescue operations. Autologous bone grafting is constrained by limited donor site availability [9,10], while allografts pose risks of disease transmission and immune rejection [11,12]. Synthetic bone materials have emerged as promising alternatives for addressing bone defects. With advances in three-dimensional (3D) printing technology and material science within bone tissue engineering, artificial bone scaffolds now exhibit performance characteristics approaching those of autologous bone in certain aspects [13–15]. Seawater-immersed wounds are associated with tissue necrosis, infection, prolonged healing period, and high mortality because of high salinity, hyperosmosis, and the presence of various pathogenic bacteria in seawater [16]. The complex interaction of these factors complicates the repair of both open wounds and bone injuries, necessitating the development of specialized materials and technologies to effectively address these challenges.

Beta-tricalcium phosphate (β-TCP) has been widely used in bone repair applications due to its chemical composition, which closely mimics natural bone tissue. It demonstrates excellent biocompatibility and osteoconductivity, providing a scaffold for bone cells to adhere, migrate, and proliferate, while also exhibiting osteoinductive properties that promote the differentiation of undifferentiated stem cells into osteoblasts [17–19]. As β-TCP degrades, it releases calcium and phosphate ions, which not only provide essential mineral support but also stimulate osteoblast activity by modulating the local microenvironment [20,21]. Additionally, the porous structure of β-TCP encourages vascularization and the ingrowth of new bone tissue, significantly enhancing bone repair quality [22]. Compared to other widely used materials, such as hydroxyapatite, β-TCP's higher degradation rate aligns more closely with the rate of bone regeneration, thereby reducing the risk of complications associated with residual materials [23]. Additionally, β-TCP can be loaded with osteogenesis-promoting, anti-infective, or anti-tumor drugs or factors, which are locally released post-implantation to further enhance bone regeneration and repair defects [24,25]. The integration of β-TCP with 3D printing technologies has recently introduced innovative approaches for the personalized design and precise fabrication of bone repair scaffolds [26–28]. While the benefits of β-TCP in bone repair are well established, the specific properties and therapeutic effects of 3D-printed nano-β-TCP scaffolds for repairing seawater-immersed bone defects have not been extensively studied. This research utilized SLA-based 3D printing technology to fabricate scaffolds with a three-dimensional structure and pore sizes of approximately 400 μm. This method preserves the rough surface features conducive to cell adhesion and osteoinduction, along with the physicochemical properties of nano-β-TCP. The study aims to evaluate the scaffold characteristics, drug-loading capacity, controlled release properties, and antibacterial effects, as well as to assess their therapeutic efficacy in repairing seawater-immersed ulnar bone defects in a rabbit model. The objective is to offer valuable insights into the treatment and repair of bone defects resulting from seawater immersion.

Materials and Methods

Preparation of 3D-Printed Nano β-TCP Scaffolds

To achieve different experimental objectives, two types of 3D-printed nano β-TCP scaffolds with distinct specifications were fabricated using SLA technology: The performance testing group (5 mm diameter, 2 mm height; Fig. 1**A**) and the animal experiment group (0.5 cm diameter, 0.5 cm height; Fig. 1**B**). The main steps for SLA-based scaffold fabrication were as follows: (1) Preparation of the photosensitive resin pre-mixture: A blend consisting of 25 wt % epoxy acrylate and 25 wt % polyester acrylate as oligomers, 24 wt % trimethylolpropane triacrylate and 20 wt % 1, 6-hexanediol diacrylate as reactive diluents, 2 wt % photoinitiator 819, 1 wt % photoinitiator 1173, and 2 wt % Diphenyl (2,4,6-trimethylbenzoyl) phosphine oxide as photoinitiators, and 1 wt % ethyl 4-dimethylaminobenzoate as a sensitizer was prepared. The mixture was stirred for 20 min using a magnetic stirrer; (2) Preparation of the photocurable 3D printing ceramic slurry: The photosensitive resin pre-mixture from Step 1 was combined with nano β-TCP powder (purity $\geq$98 %, Batch No.: C139912, Shanghai Aladdin Biochemical Technology Co., Ltd., Shanghai, China) in a 1:1 weight ratio, along with a dispersant. The resulting mixture was placed in a ball mill and processed at 200 rpm for 10 hours to obtain a homogeneous ceramic resin slurry; (3) Photocuring 3D printing: The ceramic resin slurry from Step 2 was loaded into a photocuring 3D printer (Batch No.: CH-2019-3DD-B009-R1, 3D Discovery, RegenHU, Villaz-Saint-Pierre, Fribourg, Switzerland) operating at a 405 nm wavelength. Printing was performed layer by layer with a 50 μm layer thickness and a 4-second exposure time per layer, resulting in a green ceramic body; (4) Debinding and sintering: The green ceramic bodies from Step 3 were de-supported and subjected to debinding and sintering in a muffle furnace. The temperature was gradually increased at a rate of 5 °C/min to 1100 °C, where it was maintained for 8 hours before cooling within the furnace. The final scaffolds exhibited high density, rough surface characteristics, and osteoinductive properties as porous bioceramic nano β-TCP scaffolds [29,30].

Performance Testing of β-TCP Scaffolds

The Scanning Electron Microscope Analysis of the Scaffold

The performance testing group scaffolds were thoroughly dried, fixed onto a sample holder using conductive tape or double-sided adhesive, and then coated with a 10 nm gold film via ion sputtering. The scaffold structure was examined and photographed under a scanning electron microscope (SEM, FEI Quanta250, Batch No.: 5112-02, FEI Company, Hillsboro, OR, USA) for image analysis.

X-Ray Diffraction Analysis

After drying, X-ray diffraction (XRD) analysis (using D8 ADVANCE, Batch No.: BD73000355-01, Bruker Corporation, Karlsruhe, Germany) was conducted to evaluate the scaffold performance.

Compression Strength Analysis of the Scaffold

A microcomputer-controlled electronic universal testing machine (ETM204C, Batch No.: 17007656, Beijing Boyi Experimental Instrument Co., Ltd., Beijing, China) was used to apply pressure at a rate of 0.5 mm/min to a cylindrical scaffold from the performance testing group, ensuring correct orientation of the top and bottom. The force-displacement curve was generated, and the compressive strength and stiffness of the scaffolds were calculated.

In Vivo Slow-Release Vancomycin of the Scaffold Material in Rats

To prepare control group scaffolds, calcium sulfate powder (Batch No.: 10101-41-4, Biocomposites Ltd., St. Asaph, UK) was placed into a 5 mm × 2 mm mold cavity, followed by the addition of 20 μL of a 50 mg/mL vancomycin solution (Batch No.: 1404-93-9, Solarbio Co., Ltd., Beijing, China). The mixture was then molded and dried. To prepare experimental group scaffolds, 20 μL of a 50 mg/mL vancomycin solution was directly applied to the surface of the printed nanostructured β-TCP scaffolds, ensuring complete absorption.

Eighteen rats (Slacc Jingda Experimental Animal Co., Ltd., Changsha, China; License No. SCXK (Xiang) 2016-0002) were acclimated for 7 days prior to the experiment. Following weighing, general anesthesia was induced via intraperitoneal injection of 1 % pentobarbital sodium at a dose of 50 mg/kg. Calcium sulfate scaffolds were implanted into the left paraspinal muscles, while β-TCP scaffolds were implanted into the right paraspinal muscles. Eighteen calcium sulfate and eighteen β-TCP scaffolds were implanted, and tissue samples were collected at six time points (3, 7, 14, 28, 42, and 56 days), with three replicates per time point for averaging. Each sample comprised 0.5 g of muscle tissue from both sides of the lumbar spine of the rats. After adding phosphate-buffered saline (PBS) and shaking, the mixture was centrifuged at 3000 r/min to obtain the supernatant. The supernatant was then centrifuged again at 12000 r/min to remove further impurities, and the final supernatant was collected. Next, 25 % trichloroacetic acid was added to the collected supernatant, shaken, and centrifuged at 15000 r/min. The supernatant was then used for absorbance detection.

Vancomycin and BMP-2 were Adsorbed on the β-TCP Scaffold in the Animal Experimental Group

Under sterile conditions in a laminar flow hood, the scaffolds were placed in a 96-well plate. Each scaffold received 20 μL of vancomycin solution (50 mg/mL) and 10 μL of bone morphogenetic protein-2 (BMP-2) solution (0.1 μg/μL). The scaffolds were then allowed to air dry naturally, facilitating the adsorption of vancomycin and BMP-2 onto the β-TCP scaffolds.

Animal Grouping and Treatment

Experimental grouping: A total of 36 nine-month-old New Zealand White rabbits (Ganzhou Institute of Animal Husbandry and Fisheries, Ganzhou, China, License No. SCXK (Gan) 2018-0009) were selected for the study. The rabbits were fed standard feed and had free access to water. Prior to surgery, all animals were fasted for 12 hours. The rabbits were randomly assigned into three groups using a random number table method: The M + SI + GS group, the M + SI + TCP group, and the M + TCP group, with 12 rabbits in each group (M = Rabbit ulnar bone defect model; SI = Seawater immersion; GS = Gelatin sponge loaded with vancomycin and BMP-2; TCP = Implantation of 3D-printed nano β-TCP scaffold loaded with vancomycin and BMP-2).

Establishment and treatment of the rabbit ulnar bone defect model: Seawater from the East China Sea was collected in advance and maintained under appropriate conditions during transportation and storage. The rabbits were anesthetized via an injection of 3 % sodium pentobarbital into the marginal ear vein at a dose of 3 mL/kg. After anesthesia, the right ulnar region was shaved, disinfected, and covered with a sterile surgical drape. A longitudinal incision of approximately 4 cm was made along the up-

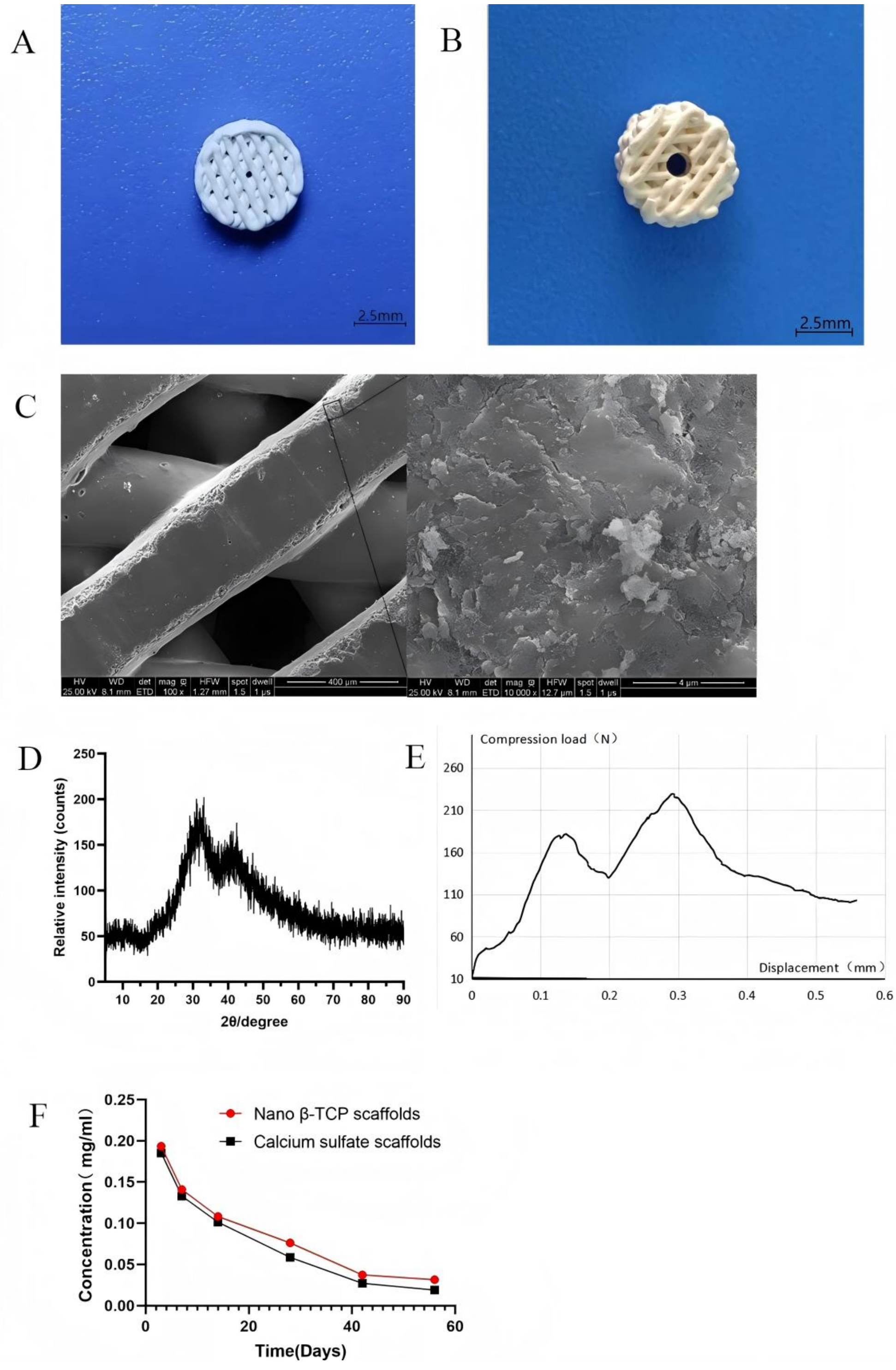

Fig. 1. Performance characteristics of the 3D-printed nano β-TCP scaffold. (**A**) Top view of the scaffold used in the performance testing group. (**B**) Top view of the scaffold used in the animal experiment group. (**C**) SEM image of the scaffold. (**D**) XRD pattern of the scaffold. (**E**) Compressive strength curve of the scaffold. (**F**) Vancomycin release profile from β-TCP and calcium sulfate scaffolds in rats (Scale bars: 2.5 mm in A and B, 400 μm and 4 μm in C; Drawing software: Adobe Photoshop 2023). TCP, tricalcium phosphate; SEM, scanning electron microscope; XRD, X-ray diffraction; 3D, three-dimensional; β-TCP, beta-tricalcium phosphate.

per part of the right forelimb ulna. The skin and subcutaneous tissue were separated to expose the ulna, and the periosteum was stripped. A 1.5 cm segment in the middle of the ulna was marked with a ruler and removed using a dental drill. The M + SI + GS and M + SI + TCP groups were immersed in seawater for 2 hours within 8 hours after surgery, while the M + TCP group was not immersed in seawater. Following successful modeling, the rabbits were

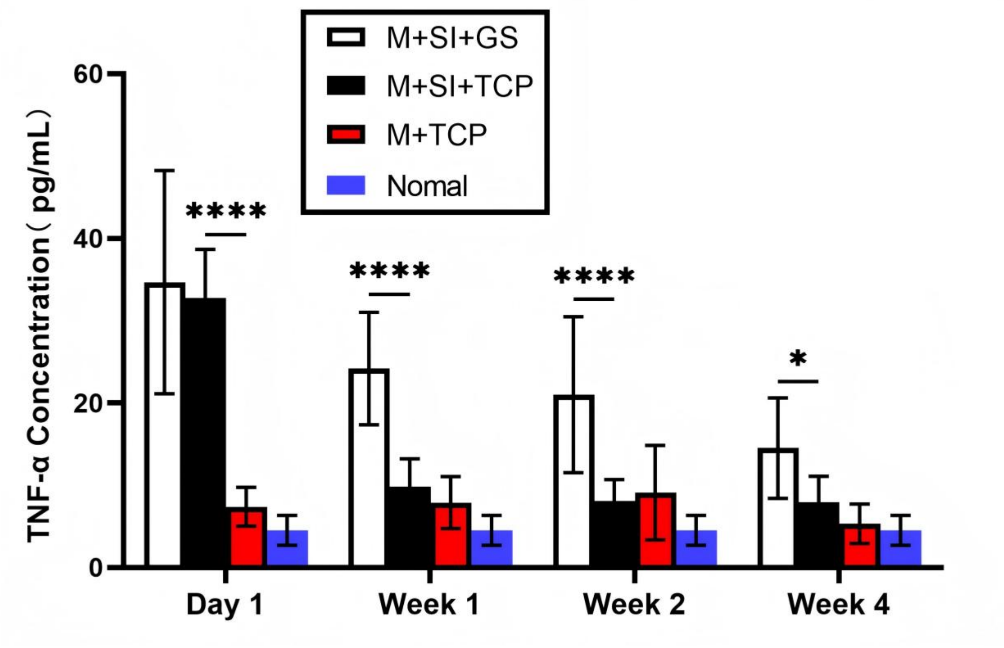

Fig. 2. Bar chart comparing serum TNF-α levels between normal rabbits and scaffold-implanted experimental rabbits at 1 day before and at 1, 2, and 4 weeks after implantation. (N = 12; mean ± SD; $^{*}p < 0.05$, $^{****}p < 0.0001$; Statistical analysis: Two-way ANOVA; Drawing software: GraphPad Prism 9.5). SD, standard deviation; TNF-α, tumor necrosis factor-alpha; ANOVA, analysis of variance.

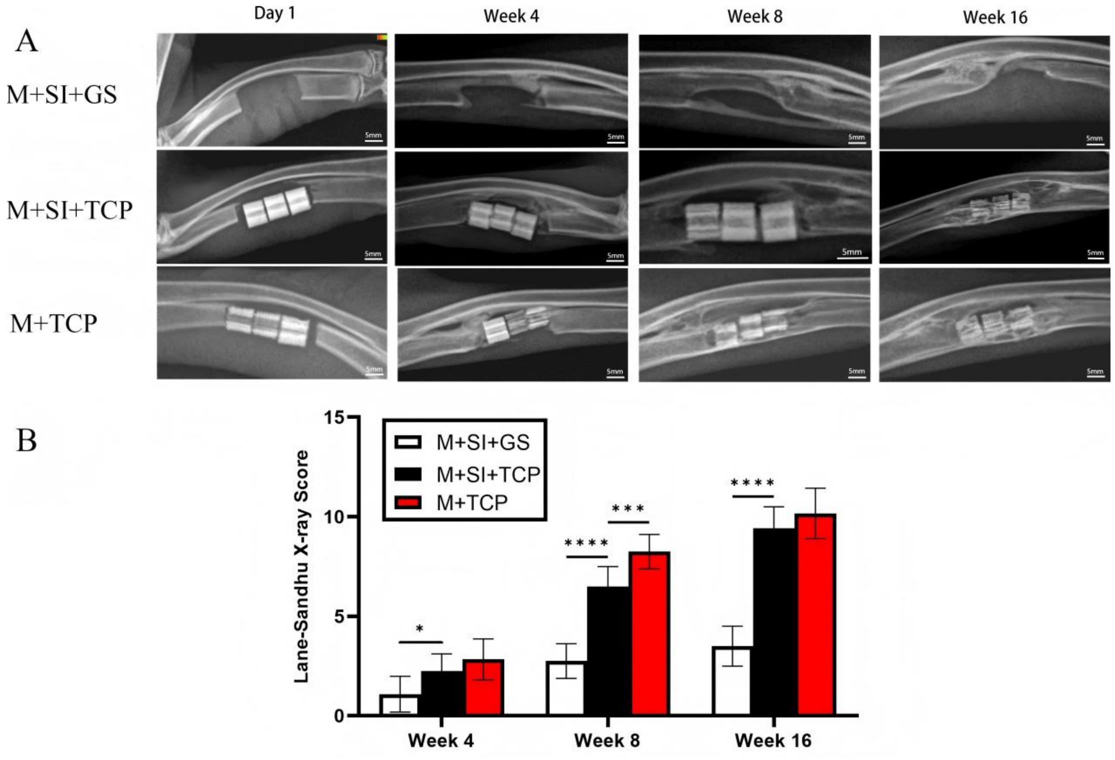

Fig. 3. Representative postoperative X-ray images and quantitative bar chart analysis of the bone defect model. (**A**) Representative X-ray images of the bone defect areas in each group at 1 day, 4 weeks, 8 weeks, and 16 weeks after implantation. (**B**) Bar chart comparing Lane-Sandhu X-ray scores at different postoperative time points among groups (Scale bars: 5 mm; n = 12; mean ± SD; $^{*}p < 0.05$, $^{***}p < 0.001$, $^{****}p < 0.0001$; Statistical analysis: Two-way ANOVA; Drawing software: GraphPad Prism 9.5 and Adobe Photoshop 2023). SD, standard deviation.

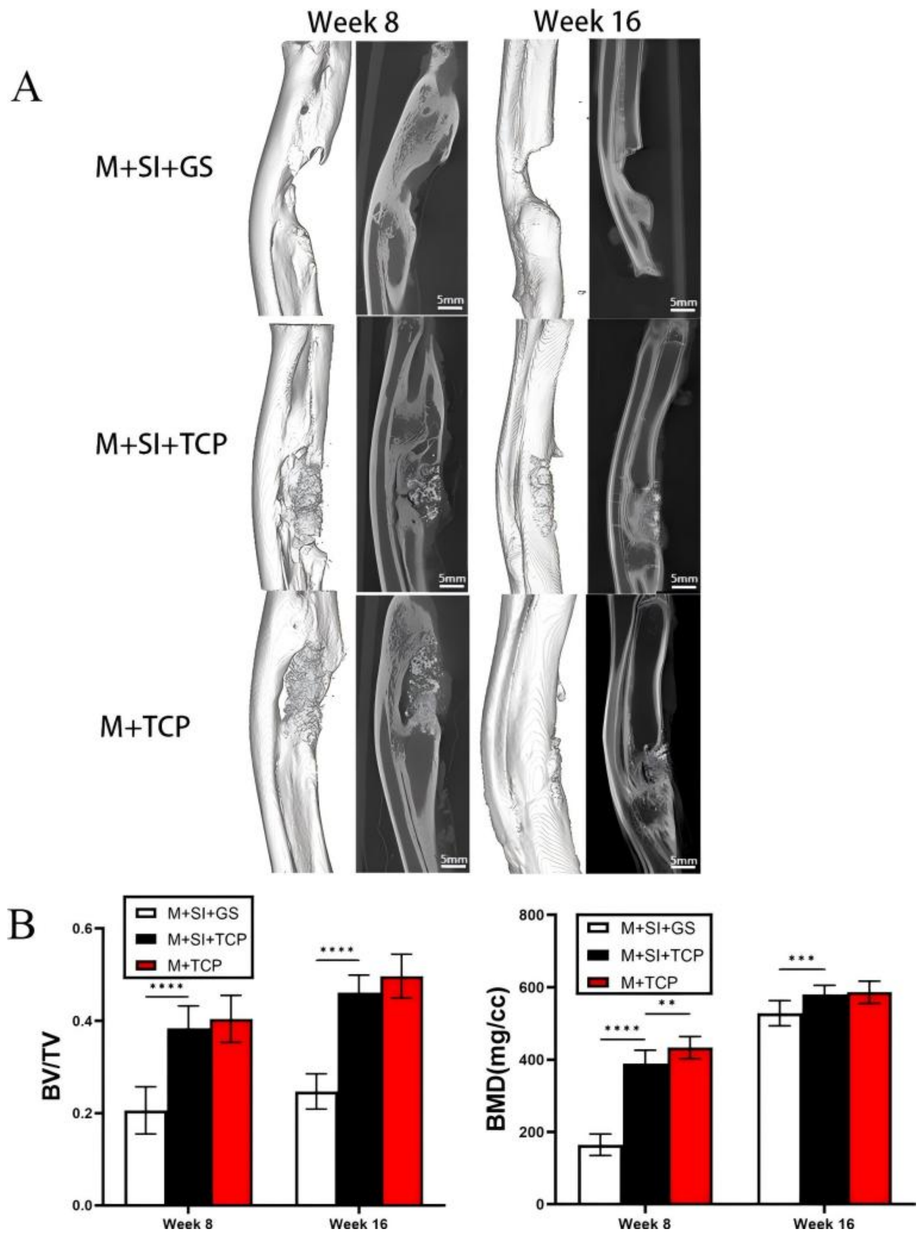

Fig. 4. Representative postoperative micro-CT images and quantitative analysis of the bone defect model. (**A**) Representative 3D micro-CT images of bone defect regions in each group at 8 and 16 weeks post-implantation. (**B**) Bar charts comparing BV/TV and BMD among groups at 8 and 16 weeks postoperatively (Scale bars: 5 mm; n = 12; mean ± SD; $^{**}p < 0.01$, $^{***}p < 0.001$, $^{****}p < 0.0001$; Statistical analysis: Two-way ANOVA; Drawing software: GraphPad Prism 9.5 and Adobe Photoshop 2023). SD, standard deviation; BV, bone volume; TV, total volume; BMD, bone mineral density; CT, computed tomography.

housed individually in cages, fed according to a standardized protocol, and received daily intramuscular injections of 800,000 units of penicillin sodium and 0.1 g of gentamicin sulfate for 5–7 days post-operation. The wound was observed daily, disinfected, and dressed. After three consecutive debridements without bacterial infection, further treatment was performed. To establish a clear baseline for natural healing and highlight the potential advantages of TCP materials in bone repair, the M + SI + GS group underwent debridement as needed within 5–7 days post-surgery, followed by filling with a gelatin sponge loaded with vancomycin and BMP-2. In both the M + TCP group and the M + SI + TCP group, the wound was debrided and a 3D-printed nano β-TCP scaffold loaded with vancomycin and BMP-2 was implanted within 5–7 days post-surgery. After filling, the incisions were sutured layer by layer, disinfected with iodine, and gentamicin sulfate was injected to prevent infection. The limbs were then immobilized with a plaster cast.

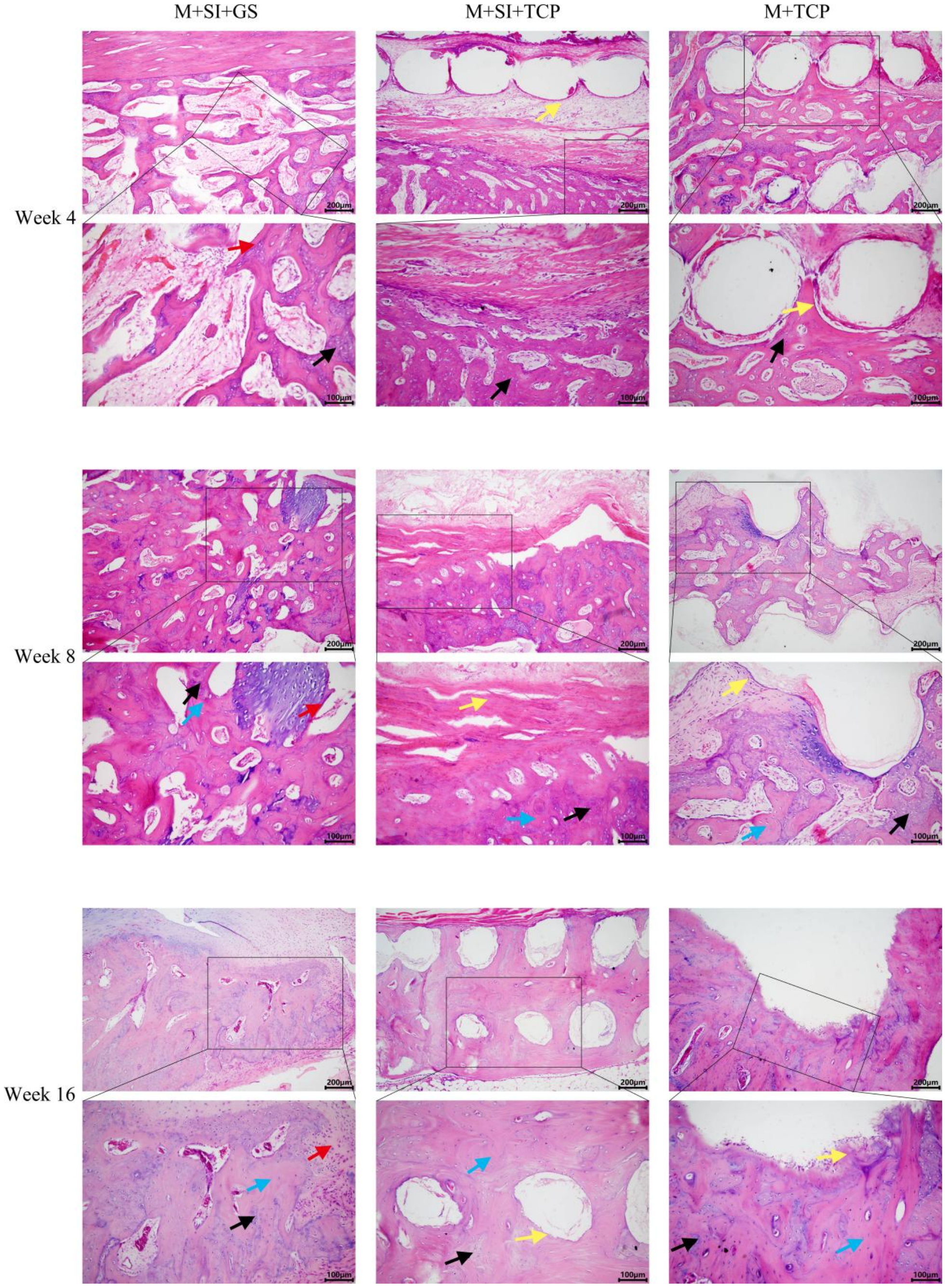

Fig. 5. Representative H&E-stained histological sections of bone defect regions from each group after surgery. Scale bars: 200 μm (upper panels) and 100 μm (lower panels); yellow arrows: Scaffold; black arrows: Newly formed bone; blue arrows: Mature bone; red arrows: Fibrous connective tissue; Drawing software: Adobe Photoshop 2023. H&E, hematoxylin-eosin.

Detection of Inflammatory Cytokines

Venous blood was collected from the marginal ear vein of New Zealand rabbits 1 day before scaffold implantation and at 1 week, 2 weeks, and 4 weeks post-implantation. The blood samples were centrifuged to isolate serum, which was stored at –80 °C. Once all samples were collected, the expression levels of the pro-inflammatory cytokine tumor necrosis factor-alpha (TNF-α) in each group were evaluated simultaneously using a specific enzyme-linked immunosorbent assay (ELISA) kit (Batch No.: 121827008102681218, Shanghai Jianglai Biotechnology Co., Ltd., Shanghai, China). Additionally, serum samples from a group of healthy New Zealand rabbits raised under identical environmental conditions were collected to measure TNF-α expression levels, serving as the positive reference control group.

X-Ray Imaging and Evaluation of the New Bone Area

Bone healing outcome was quantitatively assessed using the Lane-Sandhu X-ray scoring [31]. X-rays were taken

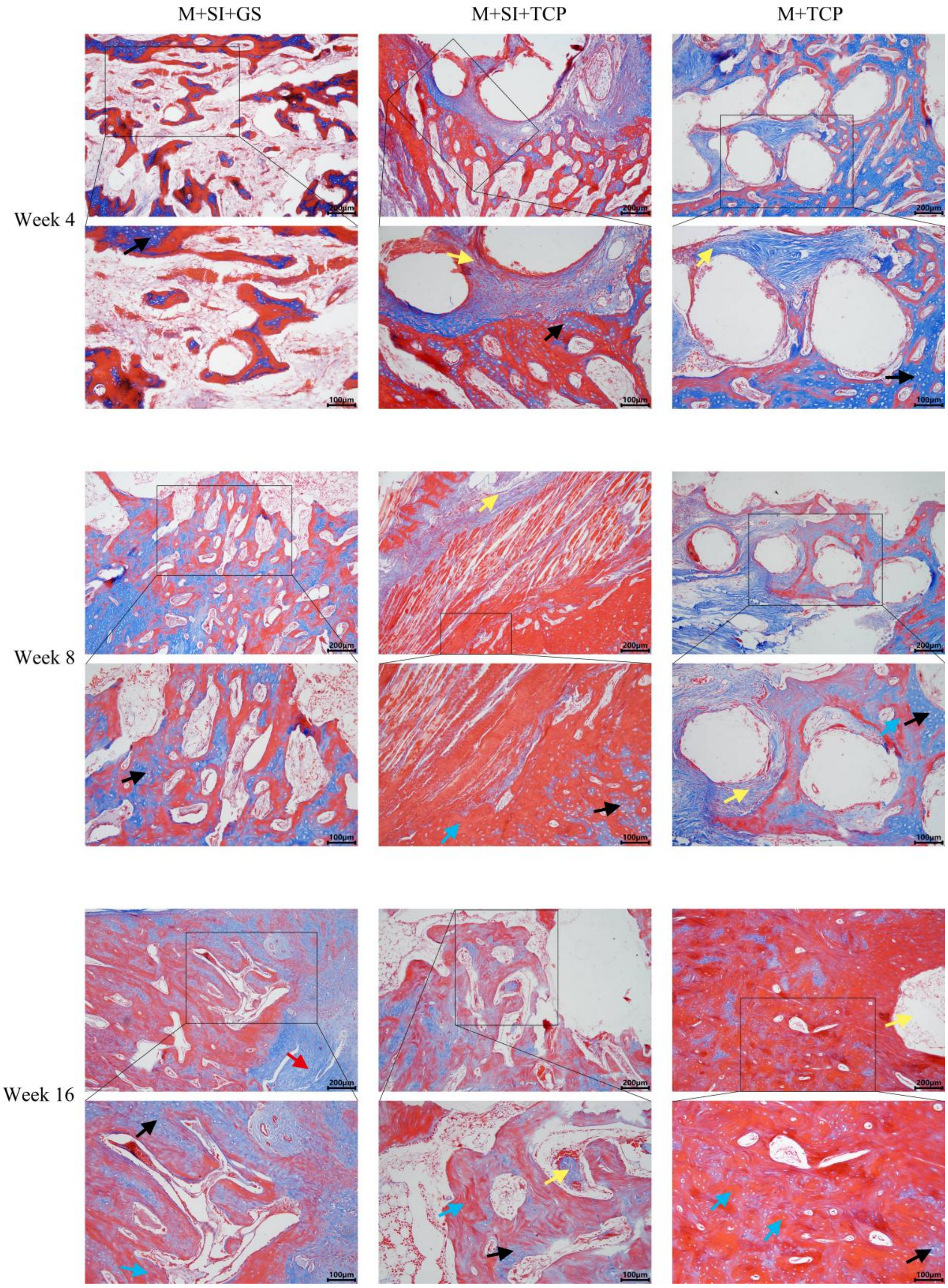

Fig. 6. Representative Masson's trichrome-stained histological sections of bone defect regions from each group after surgery. (Scale bars: 200 μm (upper panels) and 100 μm (lower panels); yellow arrows: Scaffold; black arrows: Newly formed bone; blue arrows: Mature bone; red arrows: Fibrous connective tissue; Drawing software: Adobe Photoshop 2023).

at 4 weeks, 8 weeks, and 16 weeks post-surgery, and the anteroposterior radiographs of each group were scored accordingly.

Micro-CT Evaluation

Micro-computed tomography (micro-CT) was employed to assess new bone formation. At 8 weeks and 16 weeks post-surgery, the collected bone specimens were scanned using micro-CT (Batch No.: H010-201912NC03, Bruker SkyScan, Kontich, Belgium) at a resolution of 20.4 μm for all bone defect areas. A threshold of $>$1200 was used to identify bone tissue, while a threshold of $<$1200 was used to distinguish bone marrow, soft tissue, and implanted scaffolds. New bone formation was evaluated based on bone mineral density (BMD), total volume (TV), and bone volume (BV).

Histology and Immunohistochemistry

At 4, 8, and 16 weeks post-surgery, rabbits were euthanized by injecting 20 mL of air through the ear vein. The

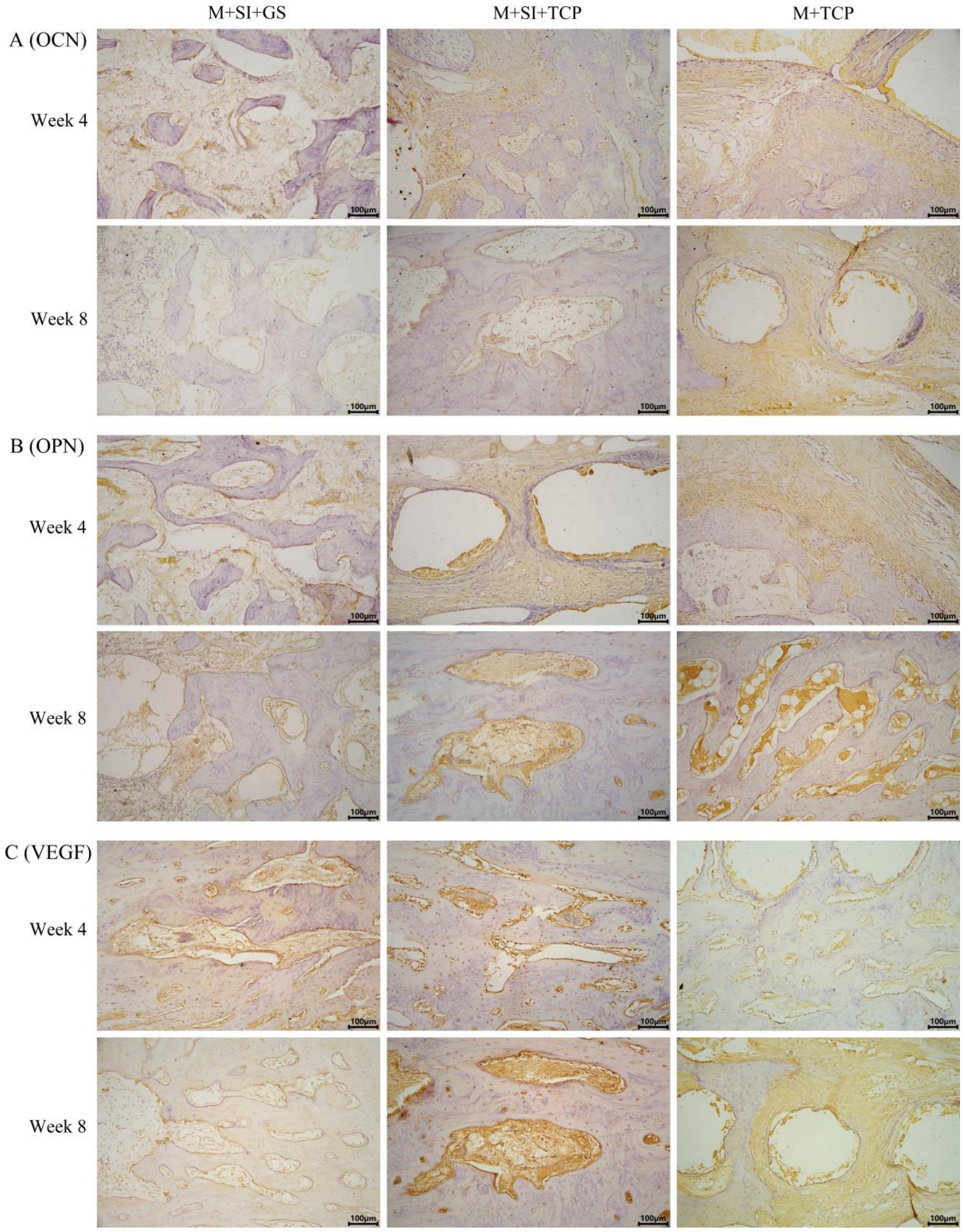

Fig. 7. Immunohistochemical staining of osteogenic markers in histological sections of bone defect regions from each group at 4 and 8 weeks postoperatively. (**A**) Immunohistochemical staining for OCN. (**B**) Immunohistochemical staining for OPN. (**C**) Immunohistochemical staining for VEGF (Scale bar = 100 μm; Drawing software: Adobe Photoshop 2023). OCN, osteocalcin; OPN, osteopontin; VEGF, vascular endothelial growth factor.

affected ulnar specimens were immediately surgically removed. A 10 mm bone segment from the defect site was fixed in 10 % formalin, decalcified, dehydrated, and embedded in paraffin to prepare 5 μm thick sections. These sections were subjected to hematoxylin-eosin (H&E) staining and Masson staining and observed under an optical microscope (BX43, Batch No.: 9J49715-201909, Olympus, Sendai, Miyagi Prefecture, Japan). Immunohistochemical staining was then performed on the sections to detect the expression of bone repair-related proteins, including osteocalcin (OCN), osteopontin (OPN), and vascular endothelial growth factor (VEGF). Semi-quantitative analysis was conducted using ImageJ software (ImageJ2 2.17.0, National Institutes of Health, Bethesda, MD, USA).

In Vitro Antibacterial Activity Assessment of the Scaffold

Following the scaffold preparation procedures described above, both the 3D-printed nano β-TCP scaffolds loaded with vancomycin and BMP-2, as well as the gelatin sponge loaded with vancomycin and BMP-2, were tested for their antibacterial properties. The scaffolds were co-cultured with *Escherichia coli (E. coli)* and *Staphylococcus aureus (S. aureus)* in appropriate growth media. Control

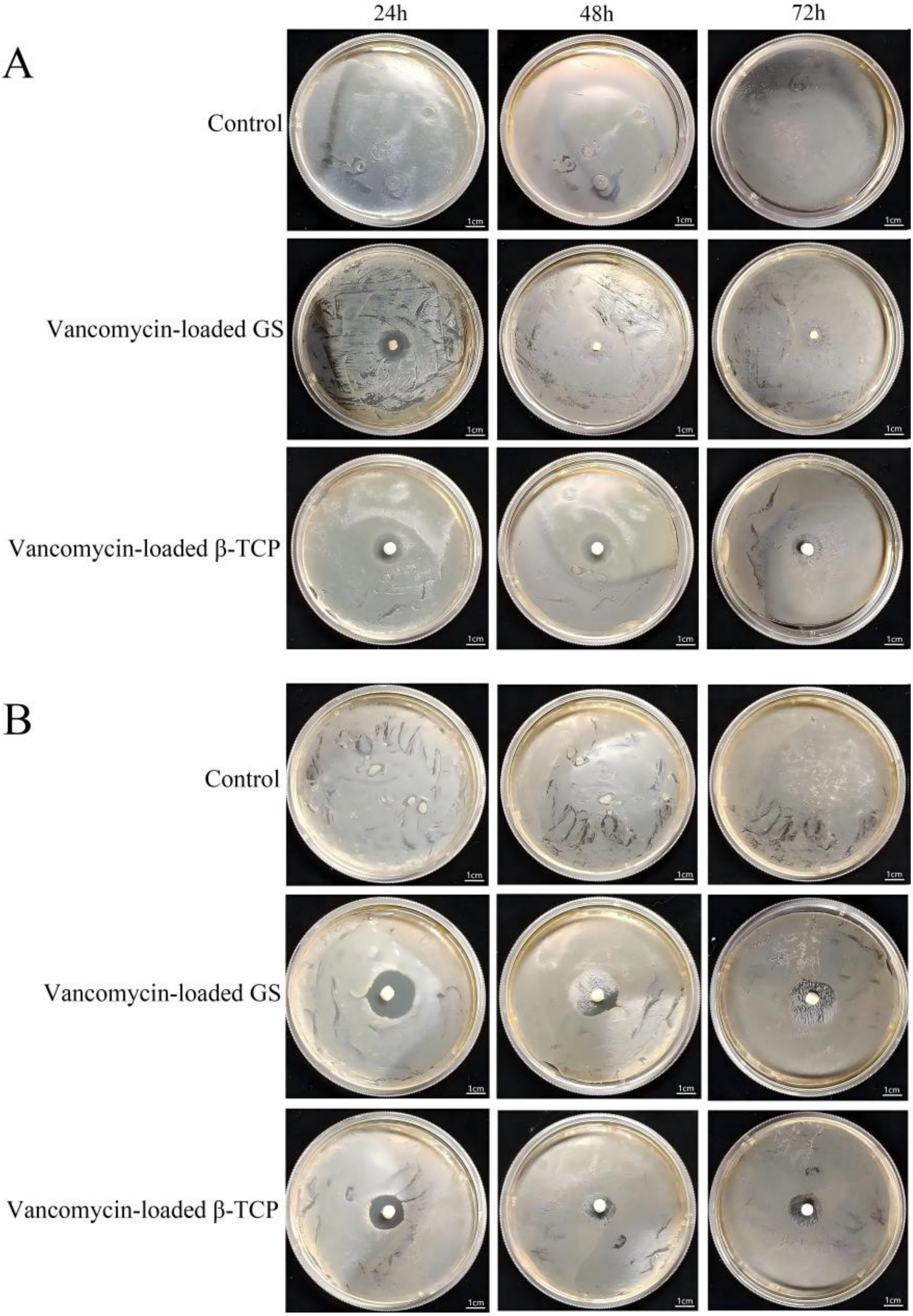

Fig. 8. Antibacterial evaluation of scaffolds *in vitro*. (**A**) Evaluation of scaffold antibacterial activity against *Escherichia coli*. (**B**) Evaluation of scaffold antibacterial activity against *Staphylococcus aureus* (Scale bar = 1 cm; Drawing software: Adobe Photoshop 2023).

groups consisted of media containing only *E. coli* or *S. aureus*. Bacterial growth was assessed at 24, 48, and 72 hours post-culture.

Statistical Methods

Quantitative data conforming to a normal distribution were presented as mean ± standard deviation (SD). Comparisons among multiple groups were performed using two-way analysis of variance (ANOVA) with GraphPad Prism 9.5 (Graph-Pad Software, San Diego, CA, USA). Grouped and paired sample data were analyzed using independent and paired *t*-tests with SPSS software, version 25.0 (IBM Corporation, Armonk, NY, USA). Statistical significance was set at $p < 0.05$.

Results

Performance Testing Results of the β-TCP Scaffold

The β-TCP scaffold exhibited a cylindrical shape with a diameter of 0.5 cm and a height of 0.5 cm, featuring a porous structure (Fig. 1**B**). SEM analysis revealed that the pore size was approximately 400 μm, with the scaffold composed of β-TCP powder and a rough surface texture (Fig. 1**C**). The scaffold had a porosity of approximately 53 %. XRD analysis showed a prominent peak at 30°, confirming the crystalline nature of the β-TCP scaffold (Fig. 1**D**). Compressive strength testing demonstrated a maximum load of 230 N, with a compressive strength of 9.6 MPa and stiffness of approximately 1800 N/mm. Under conditions preserving the scaffold's morphology, the maximum load was around 170 N, corresponding to a compressive strength of approximately 5 MPa (Fig. 1**E**).

The vancomycin release standard curve displayed a linear relationship between the vancomycin concentration and the absorbance at 280 nm. The release curves for the two types of scaffolds exhibited statistically significant differences ($p < 0.05$), with the nano β-TCP scaffold showing superior release performance compared to the calcium sulfate scaffold (Fig. 1**F**).

Serum TNF-α Levels Pre- and Post-Operatively

On the day before scaffold implantation, no statistically significant difference was observed in serum TNF-α levels between the M + SI + GS and M + SI + TCP groups ($p > 0.05$), although both groups showed higher TNF-α levels compared to the M + TCP group ($p < 0.05$). At 1 week, 2 weeks, and 4 weeks after implantation, TNF-α levels in the M + SI + GS and M + SI + TCP groups were significantly reduced compared to preoperative day 1 ($p < 0.05$). Notably, the M + SI + TCP group exhibited significantly lower TNF-α levels than the M + SI + GS group ($p < 0.05$), while no significant difference was observed between the M + SI + TCP and M + TCP groups ($p > 0.05$). At 1 week post-implantation, TNF-α levels in the M + SI + GS and M + SI + TCP groups were significantly higher than in the positive reference group of normal rabbits ($p < 0.05$), while no significant difference was found in the M + TCP group ($p > 0.05$; Fig. 2).

Bone Defect Repair Effect—X-Ray Scoring

As shown in Fig. 3, the M + SI + GS group exhibited dispersed bone structures in the defect area, with progressively deformed bone structures forming from 4 weeks postoperatively. In contrast, both the M + SI + TCP and M + TCP groups began to develop bone structures with clear bridging starting at 4 weeks post-surgery. By 16 weeks postoperatively, significant scaffold degradation was observed, with substantial mature, dense bone tissue filling the defect site. The Lane-Sandhu X-ray scores at 4, 8, and 16 weeks post-surgery were significantly higher in the M + SI + TCP and M + TCP groups compared to the M + SI + GS group ($p < 0.05$). Although the M + TCP group had a higher score than the M + SI + TCP group at 8 weeks post-surgery ($p < 0.05$), no significant difference was observed between the M + TCP group and the seawater group at 16 weeks ($p > 0.05$) (Fig. 3).

Measurement of Newly Formed Bone via Micro CT

The 3D images obtained from micro-CT reconstruction (Fig. 4) show new bone formation at 8 and 16 weeks post-implantation. At both 8 and 16 weeks, the BV/TV and BMD in the M + SI + TCP and M + TCP groups were significantly higher than those in the M + SI + GS group ($p < 0.05$). Although the BMD in the M + SI + TCP group was lower than in the M + TCP group at 8 weeks post-surgery, no significant difference in BMD was observed between the two groups at 16 weeks post-surgery ($p > 0.05$). This could be attributed to the delayed local new bone formation caused by seawater immersion. At each time point, more distinct and dense bone bridging was observed in the M + SI + TCP and M + TCP groups compared to the M + SI + GS group.

Histological Analysis of New Bone Formation

Figs. 5,6 present the histological analysis of the defect areas using H&E and Masson staining, respectively, at 4, 8, and 16 weeks post-implantation. At 4 and 8 weeks, both the M + SI + TCP and M + TCP groups exhibited significant new bone formation around the scaffolds. In contrast, the M + SI + GS group displayed minimal new bone formation with a notable presence of fibrous tissue within the defect area. By 16 weeks, the M + SI + TCP and M + TCP groups demonstrated extensive bridging and mature, dense bone tissue surrounding the scaffolds. The M + SI + GS group, however, showed scattered mature bone interspersed with fibrous structures. In scaffold-implanted defect areas, new bone tissue was deposited directly on the porous scaffold surfaces, with osteoblast-like cells aligned along the surface of the newly formed bone, contributing to bone matrix formation within the scaffold. Both H&E and Masson staining confirmed that new bone growth occurred within the pores of both scaffold types, illustrating their effective bone conduction and induction properties. Furthermore, Masson's trichrome staining (Fig. 6) indicated that, at 16 weeks, the M + TCP group exhibited significantly more new bone compared to the M + SI + TCP group, suggesting that seawater immersion may delay local bone healing.

Immunohistochemical Staining of Osteogenic Markers

Immunohistochemical analysis was conducted to assess the impact of the implanted scaffolds on osteogenic marker levels in seawater-immersed rabbit ulnar bone defects (Fig. 7, **Supplementary Fig. 1**). The results revealed that at 4, 8, and 16 weeks post-surgery, both the M + SI + TCP and M + TCP groups exhibited significantly higher levels of OCN, OPN, and VEGF compared to the M + SI + GS group (**Supplementary Fig. 2A**). These findings suggest that the 3D-printed nano β-TCP scaffolds loaded with vancomycin and BMP-2 enhance new bone formation by promoting the production of osteogenic proteins.

In Vitro Antibacterial Evaluation of 3D-Printed Nano β-TCP Scaffolds

In vitro antibacterial tests were conducted to evaluate the efficacy of β-TCP scaffolds loaded with vancomycin and BMP-2 (Vancomycin + β-TCP) in comparison to gelatin sponges loaded with vancomycin and BMP-2 (Vancomycin + GS) (Fig. 8). The results showed the following: *E. coli*: The Vancomycin + GS group exhibited a reduction in the inhibition zone at 48 hours, indicating a decrease in antibacterial activity. In contrast, the Vancomycin + β-TCP group maintained a stable inhibition zone at 72 hours with no significant reduction, demonstrating superior antibacterial efficacy (Fig. 8**A**). *S. aureus*: The Vancomycin + GS group also showed a decrease in the inhibition zone at 72 hours, suggesting diminished antibacterial activity. Conversely, the Vancomycin + β-TCP group continued to exhibit a consistent inhibition zone at 72 hours, indicating sustained and effective antibacterial performance (Fig. 8**B**). These results highlight that Vancomycin + β-TCP scaffolds offer more reliable and prolonged antibacterial activity compared to Vancomycin + GS gelatin sponges (**Supplementary Fig. 2B**).

Discussion

The treatment of bone defects resulting from seawater immersion requires addressing both the injury caused by the seawater and the infection, in addition to the bone defect itself. With advancements in bone tissue engineering and material science, the biocompatibility and tissue compatibility of artificial bone graft materials have significantly improved, enabling them to increasingly replace autogenous and allogeneic bone grafts in clinical applications [32,33]. An ideal bone material is generally agreed to have the following characteristics: good biocompatibility [34]; non-toxicity and non-immunogenicity, indicating that it should not induce immune rejection when implanted [35]; strong plasticity, allowing it to be easily modified during surgery to fit various bone defect shapes [36]; sufficient biomechanical strength with self-supporting mechanical properties [37]; moderate biodegradability [38]; appropriate pore size, porosity, and connectivity while providing essential cell factors for growth and differentiation, such as VEGF and bone morphogenetic proteins [39,40]. Furthermore, it should possess both bone induction and conduction properties, meaning it can induce or guide tissue regeneration, facilitate the rapid invasion of vessels and stromal cells, and gradually remodel and absorb during the new bone growth process, eventually disappearing from the implantation site [41,42]. Given these requirements, our research team selected nano β-TCP as the material for scaffold printing, functionalizing it by loading BMP-2 and vancomycin. This approach not only facilitates the repair of large bone defects but also provides local, sustained release of vancomycin to address the heightened infection risk associated with seawater immersion injuries.

In this study, a 3D printing method based on SLA technology was employed, using a photosensitive resin premixture followed by photopolymerization, debinding, and sintering. The resulting 3D-printed nano β-TCP scaffold exhibited a rough surface conducive to cell adhesion and osteoinductive properties, along with high internal precision, consistent material structure, and stable physicochemical properties. According to preoperative 3D printing design and electron microscopy analysis, the scaffold had a porosity of approximately 53 %, with an internal pore size of around 400 μm, high interconnectivity, and an organized structure. These features create favorable conditions for bone cells and blood vessels to infiltrate the scaffold upon implantation into the bone defect area. The pressure curve analysis indicated that the scaffold had a stiffness of approximately 1800 N/mm and a maximum compressive strength of 5 MPa without deformation. This is equivalent to a pressure of 1742.7 N on a 4 cm diameter femoral cortical bone (with a cortical thickness of 3 mm), which is 2.5 times the average body weight of a person, fully meeting the requirements for normal standing. Given the rapid degradation and absorption of the implanted gelatin sponge, clinically used calcium sulfate artificial bone was selected as the control group for the vancomycin sustained-release experiment in rats. The results suggested that the vancomycin loading capacity of the scaffold was comparable to that of calcium sulfate, but with superior sustained release capabilities, extending over 56 days. As noted in research of Kitahara *et al* [43], β-TCP composite scaffolds loaded with BMP-2 also demonstrate excellent sustained release properties, consistently releasing BMP-2 over a three-week period. This extended release facilitates continuous bone formation, particularly in scenarios where bone healing requires prolonged periods, such as in nonunion cases. Furthermore, the printing method employed offers high reproducibility, fulfilling the essential criteria for producing ideal bone graft materials. However, limitations in our material preparation methods led to differences in the drug loading approach between the scaffold and calcium sulfate in the *in vivo* release experiments, which introduces some constraints on the interpretation of our drug release results.

In the experiment investigating scaffold repair of seawater-soaked ulnar defects in rabbits, serum TNF-α levels in both the M + SI + GS and M + SI + TCP groups one day prior to scaffold implantation were significantly higher than in the M + TCP group ($p < 0.05$), indicating that seawater exposure to bone defects stimulates the release of inflammatory cytokines. After scaffold implantation, the serum TNF-α levels in the M + SI + TCP group were significantly lower than those in the M + SI + GS group ($p < 0.05$) and showed no significant difference compared to the M + TCP group ($p > 0.05$), highlighting the scaffold's excellent anti-inflammatory properties. Furthermore, serum TNF-α levels in the M + TCP group did not show a significant increase post-surgery when compared to pre-implantation levels, suggesting that the scaffold does not promote the release of inflammatory cytokines. Cen *et al*. [44] previously conducted an *in vitro* evaluation of 3D-printed composite scaffolds containing 15 % β-TCP, demonstrating their anti-inflammatory mechanism. The study revealed that the scaffold encourages the polarization of M0 macrophages to the M2 phenotype, leading to increased secretion of the anti-inflammatory cytokine IL-10 and growth factors such as VEGF and BMP-2. Postoperative X-ray imaging and micro-CT scans were used to evaluate bone tissue repair effectiveness in the defect areas. X-ray imaging showed that, compared to the M + SI + GS group, both the M + SI + TCP and M + TCP groups exhibited significantly greater new bone formation bridging the defects ($p < 0.05$). However, at 8 weeks post-surgery, the Lane-Sandhu X-ray scores for the M + SI + TCP group were lower than those for the M + TCP group ($p < 0.05$), while at 16 weeks post-surgery, no significant differences were observed between the two groups. This difference may be attributed to ischemia, hypoxia, and edema caused by seawater exposure, which could affect bone defect repair. At 16 weeks post-surgery, scaffolds in both the M + SI + TCP and M + TCP groups had begun to degrade, with substantial new bone tissue ingrowth, indicating that the scaffold degrades in parallel with bone defect repair. Micro-CT analysis revealed that, compared to the M + SI + GS group, both the M + SI + TCP and M + TCP groups demonstrated significantly greater new bone formation at the defect sites post-surgery, suggesting enhanced scaffold-mediated repair of seawater-soaked bone defects. Histological analysis also showed increased new bone formation in the M + SI + TCP and M + TCP groups relative to the M + SI + GS group, indicating that the 3D-printed nano β-TCP scaffolds loaded with vancomycin and BMP-2 could improve the repair of seawater-soaked bone defects. Immunohistochemical staining revealed higher expression levels of VEGF, OCN, and OPN in the M + SI + TCP and M + TCP groups compared to the M + SI + GS group post-surgery, suggesting that the scaffolds promote new bone formation by upregulating osteogenesis-related proteins and enhancing osteogenic differentiation of bone marrow mesenchymal stem cells. *In vitro* antibacterial experiments demonstrated that the 3D-printed nano β-TCP scaffold co-loaded with vancomycin and BMP-2 exhibited excellent antibacterial efficacy against *Escherichia coli* and *Staphylococcus aureus*, potentially mitigating the high infection risk associated with seawater immersion injuries. Badwelan *et al*. [45] conducted a comparative *in vitro* study on amoxicillin release from β-TCP composite scaffolds, revealing that scaffolds containing 70 % β-TCP exhibited stronger antibacterial activity. While the drug-loaded gelatin sponge group showed larger inhibition zone diameters compared to the β-TCP group, this may be attributed to the rapid release of the drug from the gelatin sponge over a short period. In contrast, β-TCP releases the drug slowly and continuously, suggesting that drug-loaded β-TCP is more effective for sustained antibacterial action.

However, this study has certain limitations. One limitation is the lack of characterization of the bacterial species present in the East China Sea, from which the seawater was collected. While a previous study screened various bacterial communities [46], the focus of this study was primarily on evaluating the scaffold's ability to promote bone repair. Consequently, there remains significant potential to enhance the assessment of its performance through more comprehensive cellular experiments, as well as its anti-inflammatory and antibacterial capabilities. Additionally, at the final follow-up, X-ray imaging showed that the scaffold had not yet fully degraded or been absorbed, possibly due to the relatively short follow-up period. Future research will aim to include *in vitro* cellular studies, further evaluate the anti-inflammatory and antibacterial capabilities, and extend the follow-up duration to improve scaffold evaluation and explore its ultimate degradation *in vivo*.

Conclusions

In conclusion, the nano 3D-printed β-TCP scaffolds produced via SLA technology demonstrate key characteristics such as high porosity, exceptional connectivity, consistent pore sizes, and efficient drug release capabilities. These scaffolds effectively address bone defects exposed to seawater, facilitating bone tissue repair. This study provides valuable insights and serves as a reference for the clinical management of such bone defects.

List of Abbreviations

3D, three-dimensional; β-TCP, beta-tricalcium phosphate; BMP-2, bone morphogenetic protein-2; SEM, scanning electron microscope; TNF-α, tumor necrosis factor-alpha; CT, computed tomography; H&E, hematoxylin-eosin; VEGF, vascular endothelial growth factor; OCN, osteocalcin; OPN, osteopontin; SLA, stereo lithography apparatus; BMD, bone mineral density; TV, total volume; BV, bone volume; XRD, X-ray diffraction; SD, standard deviation; ANOVA, analysis of variance; *E. coli, escherichia coli*; *S. aureus, staphylococcus aureus*; PBS, phosphate-buffered saline; ELISA, enzyme-linked immunosorbent assay.

Availability of Data and Materials

Data reported in this paper will be shared by the lead contact upon request. This paper does not report original code. Any additional information required to reanalyze the data reported in this paper is available from the lead contact upon request.

Author Contributions

HDL, DL, SEL and JJZ contributed to the design of this work. RY, YNY, MZ and GSL contributed to the interpretation of data. XYN, JLG, XMC and HL analyzed the data. HDL and DL drafted the work. SEL and JJZ revised critically for important intellectual content. All authors critically reviewed the manuscript for important intellectual content. All authors read and approved the final manuscript. All authors agreed to be accountable for all aspects of the work in ensuring that questions related to the accuracy or integrity of any part of the work were appropriately investigated and resolved.

Ethics Approval and Consent to Participate

Animal experiments were approved by the Ethics Committee of the 908th Hospital, Chinese People's Liberation Army Joint Logistics Support Force (Approval No. 2019–21). All procedures were conducted in strict accordance with relevant ethical guidelines and regulatory standards. All animal experimental procedures were performed in accordance with ARRIVE guidelines 2.0.

Acknowledgments

Not applicable.

Funding

This work was supported by the PLA's High-level Talents Independently Projects (2022-17-02), Key R&D Project of Jiangxi Province (20192BBGL70010), National Natural Science Foundation of China (82272505), Natural Science Foundation of Guangdong Province (2023A1515011040), and partially supported by grants from Research Grants Council of University Grants Committee Hong Kong (14113723, 14119124, 14121721, N_CUHK472/22, T13-402/17-N and AoE/M-402/20), the National Natural Science Foundation of China (81874000).

Conflict of Interest

There are no conflicts of interest to declare.

Supplementary Material

Supplementary material associated with this article can be found, in the online version, at https://doi.org/10.22203/eCM.v052a07.

References

[1] Ye J, Miao B, Xiong Y, Guan Y, Lu Y, Jia Z, *et al*. 3D printed porous magnesium metal scaffolds with bioactive coating for bone defect repair: enhancing angiogenesis and osteogenesis. Journal of Nanobiotechnology. 2025; 23: 160. https://doi.org/10.1186/s12951-025-03222-3.

[2] Jin DS, Zhao ZH, Ruan SQ, Huang WL, Tian RY, Wan Y, *et al*. Icariin-loaded composite scaffold promotes osteogenic differentiation and bone regeneration. BMC Musculoskeletal Disorders. 2025; 26: 548. https://doi.org/10.1186/s12891-025-08824-4.

[3] Li C, Sun F, Tian J, Li J, Sun H, Zhang Y, *et al*. Continuously released Zn^{2+} in 3D-printed PLGA/β-TCP/Zn scaffolds for bone defect repair by improving osteoinductive and anti-inflammatory properties. Bioactive Materials. 2022; 24: 361–375. https://doi.org/10.1016/j.bioactmat.2022.12.015.

[4] Qin H, Weng J, Zhou B, Zhang W, Li G, Chen Y, *et al*. Magnesium Ions Promote *in Vitro* Rat Bone Marrow Stromal Cell Angiogenesis through Notch Signaling. Biological Trace Element Research. 2023; 201: 2823–2842. https://doi.org/10.1007/s12011-022-03364-7.

[5] Fang Q, Yao Z, Feng L, Liu T, Wei S, Xu P, *et al*. Antibiotic-loaded chitosan-gelatin scaffolds for infected seawater immersion wound healing. International Journal of Biological Macromolecules. 2020; 159: 1140–1155. https://doi.org/10.1016/j.ijbiomac.2020.05.126.

[6] Xiong J, Ji B, Wang L, Yan Y, Liu Z, Fang S, *et al*. Human Adipose-Derived Stem Cells Promote Seawater-Immersed Wound Healing by Activating Skin Stem Cells via the EGFR/MEK/ERK Pathway. Stem Cells International. 2019; 2019: 7135974. https://doi.org/10.1155/2019/7135974.

[7] Zhang G, Chen X, Cheng X, Ma W, Chen C. BMSC seeding in different scaffold incorporation with hyperbaric oxygen treats seawater-immersed bony defect. Journal of Orthopaedic Surgery and Research. 2021; 16: 249. https://doi.org/10.1186/s13018-021-02368-8.

[8] Wang X, Xu P, Yao Z, Fang Q, Feng L, Guo R, *et al*. Preparation of Antimicrobial Hyaluronic Acid/Quaternized Chitosan Hydrogels for the Promotion of Seawater-Immersion Wound Healing. Frontiers in Bioengineering and Biotechnology. 2019; 7: 360. https://doi.org/10.3389/fbioe.2019.00360.

[9] Faour O, Dimitriou R, Cousins CA, Giannoudis PV. The use of bone graft substitutes in large cancellous voids: any specific needs? Injury. 2011; 42: S87–S90. https://doi.org/10.1016/j.injury.2011.06.020.

[10] Castanheira EJ, Rodrigues JMM, Mano JF. Cryogels Composites: Recent Improvement in Bone Tissue Engineering. Nano Letters. 2024; 24: 13875–13887. http://doi.org/10.1021/acs.nanolett.4c03197.

[11] Ma Z, Yang Q, Liu X, Li, Z. Application of allograft and absorbable screws in the reconstruction of a massive bone defect following resection of giant osteochondroma: A retrospective study. Frontiers in Surgery. 2022; 9: 938750. https://doi.org/10.3389/fsurg.2022.938750.

[12] Archunan MW, Petronis S. Bone Grafts in Trauma and Orthopaedics. Curēus. 2021; 13: e17705. https://doi.org/10.7759/cureus.17705.

[13] Meng M, Wang J, Huang H, Liu X, Zhang J, Li Z. 3D printing metal implants in orthopedic surgery: Methods, applications and future

prospects. Journal of Orthopaedic Translation. 2023; 42: 94–112. https://doi.org/10.1016/j.jot.2023.08.004.

[14] Kennedy MM, Mikos AG. Biomaterials-based approaches to mandibular tissue engineering: where we were, where we are, where we are going. Regenerative Biomaterials. 2025; 12: rbaf024. https://doi.org/10.1093/rb/rbaf024.

[15] Wang FZ, Liu S, Gao M, Yu Y, Zhang WB, Li H, *et al*. 3D-Printed Polycaprolactone/Hydroxyapatite Bionic Scaffold for Bone Regeneration. Polymers. 2025; 17: 858. http://doi.org/10.3390/polym17070858.

[16] Lv Y, Cai F, He Y, Li L, Huang Y, Yang J, *et al*. Multi-crosslinked hydrogels with strong wet adhesion, self-healing, antibacterial property, reactive oxygen species scavenging activity, and on-demand removability for seawater-immersed wound healing. Acta Biomaterialia. 2023; 159: 95–110. http://doi.org/10.1016/j.actbio.2023.01.045.

[17] Xu S, Zhang H, Li X, Zhang X, Liu H, Xiong Y,*et al*. Fabrication and biological evaluation of porous β-TCP bioceramics produced using digital light processing. Proceedings of the Institution of Mechanical Engineers. Part H, Journal of Engineering in Medicine. 2022; 236: 286–294. https://doi.org/10.1177/09544119211041186.

[18] Lima JR, Soares PBF, Pinotti FE, Marcantonio RAC, Marcantonio-Junior E, de Oliveira GJPL. Comparison of the osseointegration of implants placed in areas grafted with HA/TCP and native bone. Microscopy Research and Technique. 2022; 85: 2776–2783. https://doi.org/10.1002/jemt.24126.

[19] Durge KJ, Baliga VS, Sridhar SB, Dhadse PV, Ragit GC. Extraction socket grafting using recombinant human bone morphogenetic protein-2-clinical implications and histological observations. BMC Research Notes. 2021; 14: 61. https://doi.org/10.1186/s13104-021-05476-0.

[20] Peng Z, Wang C, Liu C, Xu H, Wang Y, Liu Y, *et al*. 3D printed polycaprolactone/beta-tricalcium phosphate/magnesium peroxide oxygen releasing scaffold enhances osteogenesis and implanted BMSCs survival in repairing the large bone defect. Journal of Materials Chemistry. B. 2021; 9: 5698–5710. https://doi.org/10.1039/d1tb00178g.

[21] Besleaga C, Nan B, Popa AC, Balescu LM, Nedelcu L, Neto AS, *et al*. Sr and Mg Doped Bi-Phasic Calcium Phosphate Macroporous Bone Graft Substitutes Fabricated by Robocasting: A Structural and Cytocompatibility Assessment. Journal of Functional Biomaterials. 2022; 13: 123. https://doi.org/10.3390/jfb13030123.

[22] Huang M, Fan J, Ma Z, Li J, Lu Y. Establishment and biological effect evaluation of prevascularized porous β-tricalcium phosphate tissue engineered bone. Zhongguo Xiu Fu Chong Jian Wai Ke Za Zhi = Zhongguo Xiufu Chongjian Waike Zazhi = Chinese Journal of Reparative and Reconstructive Surgery. 2022; 36: 625–632. https://doi.org/10.7507/1002-1892.202202010.

[23] Tseng KF, Shiu ST, Hung CY, Chan YH, Chee TJ, Huang PC, *et al*. Osseointegration Potential Assessment of Bone Graft Materials Loaded with Mesenchymal Stem Cells in Peri-Implant Bone Defects. International Journal of Molecular Sciences. 2024; 25: 862. https://doi.org/10.3390/ijms25020862.

[24] Topsakal A, Ekren N, Kilic O, Oktar FN, Mahirogullari M, Ozkan O, *et al*. Synthesis and characterization of antibacterial drug loaded β-tricalcium phosphate powders for bone engineering applications. Journal of Materials Science. Materials in Medicine. 2020; 31: 16. https://doi.org/10.1007/s10856-019-6356-1.

[25] Jiao X, Sun X, Li W, Chu W, Zhang Y, Li Y, *et al*. 3D-Printed β-Tricalcium Phosphate Scaffolds Promote Osteogenic Differentiation of Bone Marrow-Deprived Mesenchymal Stem Cells in an N6-methyladenosine-Dependent Manner. International Journal of Bioprinting. 2022; 8: 544. https://doi.org/10.18063/ijb.v8i2.544.

[26] Zheng C, Attarilar S, Li K, Wang C, Liu J, Wang L, *et al*. 3D-printed HA15-loaded β-Tricalcium Phosphate/Poly (Lactic-co-glycolic acid) Bone Tissue Scaffold Promotes Bone Regeneration in Rabbit Radial Defects. International Journal of Bioprinting. 2021; 7: 317. https://doi.org/10.18063/ijb.v7i1.317.

[27] Cheng K, Peng Y, Diao J, Zhu H, Lu Q, Zhao N, *et al*. Personalizing β-TCP porous scaffolds to promote osteogenesis: a study of segmental femoral defects in beagle models. Biomedical Materials. 2024; 20: 015023. https://doi.org/10.1088/1748-605X/ad98d8.

[28] Zhang Y, Li M, Zhang H, You J, Zhou J, Ren S, *et al*. 3D-printed intelligent photothermal conversion Nb_2C MXene composite scaffolds facilitate the regulation of angiogenesis-osteogenesis coupling for vascularized bone regeneration. Materials Today. Bio. 2025; 31: 101647. https://doi.org/10.1016/j.mtbio.2025.101647.

[29] Wang C, Lin K, Chang J, Sun J. Osteogenesis and angiogenesis induced by porous β-CaSiO(3)/PDLGA composite scaffold via activation of AMPK/ERK1/2 and PI3K/Akt pathways. Biomaterials. 2013; 34: 64–77. https://doi.org/10.1016/j.biomaterials.2012.09.021.

[30] O'Brien CM, Holmes B, Faucett S, Zhang LG. Three-dimensional printing of nanomaterial scaffolds for complex tissue regeneration. Tissue Engineering. Part B, Reviews. 2015; 21: 103–114. http://doi.org/10.1089/ten.TEB.2014.0168.

[31] Gao C, Qiu ZY, Hou JW, Tian W, Kou JM, Wang X. Clinical observation of mineralized collagen bone grafting after curettage of benign bone tumors. Regenerative Biomaterials. 2020; 7: 567–575. https://doi.org/10.1093/rb/rbaa031.

[32] Dulany K, Hepburn K, Goins A, Allen JB. *In vitro* and *in vivo* biocompatibility assessment of free radical scavenging nanocomposite scaffolds for bone tissue regeneration. Journal of Biomedical Materials Research. Part A. 2020; 108: 301–315. http://doi.org/10.1002/jbm.a.36816.

[33] Zhao Y, Fan T, Chen J, Su J, Zhi X, Pan P, *et al*. Magnetic bioinspired micro/nanostructured composite scaffold for bone regeneration. Colloids and Surfaces. B, Biointerfaces. 2019; 174: 70–79. https://doi.org/10.1016/j.colsurfb.2018.11.003.

[34] Funayama T, Noguchi H, Kumagai H, Sato K, Yoshioka T, Yamazaki M. Unidirectional porous beta-tricalcium phosphate and hydroxyapatite artificial bone: a review of experimental evaluations and clinical applications. Journal of Artificial Organs: The Official Journal of the Japanese Society for Artificial Organs. 2021; 24: 103–110. https://doi.org/10.1007/s10047-021-01270-8.

[35] Steijvers E, Ghei A, Xia Z. Manufacturing artificial bone allografts: a perspective. Biomaterials Translational. 2022; 3: 65–80. https://doi.org/10.12336/biomatertransl.2022.01.007.

[36] Kobayashi K, Yukiue T, Yoshida H, Tsuboi N, Takahashi Y, Makino K, *et al*. Ultra-high-molecular-weight Polyethylene (UHMWPE) Wing Method for Strong Cranioplasty. Neurologia Medico-Chirurgica. 2021; 61: 549–556. https://doi.org/10.2176/nmc.oa.2021-0032.

[37] Metzner F, Neupetsch C, Carabello A, Pietsch M, Wendler T, Drossel WG. Biomechanical validation of additively manufactured artificial femoral bones. BMC Biomedical Engineering. 2022; 4: 6. https://doi.org/10.1186/s42490-022-00063-1.

[38] Li Y, Pavanram P, Bühring J, Rütten S, Schröder KU, Zhou J, *et al*. Physiomimetic biocompatibility evaluation of directly printed degradable porous iron implants using various cell types. Acta Biomaterialia. 2023; 169: 589–604. https://doi.org/10.1016/j.actbio.2023.07.056.

[39] Ren M, Wang X, Hu M, Jiang Y, Xu D, Xiang H, *et al*. Enhanced bone formation in rat critical-size tibia defect by a novel quercetin-containing alpha-calcium sulphate hemihydrate/nano-hydroxyapatite composite. Biomedicine & Pharmacotherapy = Biomédecine & Pharmacothérapie. 2022; 146: 112570. https://doi.org/10.1016/j.biopha.2021.112570.

[40] Zhang J, Wehrle E, Adamek P, Paul GR, Qin XH, Rubert M, *et al*. Optimization of mechanical stiffness and cell density of 3D bioprinted cell-laden scaffolds improves extracellular matrix mineralization and cellular organization for bone tissue engineering. Acta Biomaterialia. 2020; 114: 307–322. https://doi.org/10.1016/j.actbio

.2020.07.016.

[41] He W, Wei D, Zhang J, Huang X, He D, Liu B, *et al*. Novel bone repairing scaffold consisting of bone morphogenetic Protein-2 and human Beta Defensin-3. Journal of Biological Engineering. 2021; 15: 5. https://doi.org/10.1186/s13036-021-00258-5.

[42] Imagawa N, Inoue K, Matsumoto K, Omori M, Yamamoto K, Nakajima Y, *et al*. Histological Evaluation of Porous Additive-Manufacturing Titanium Artificial Bone in Rat Calvarial Bone Defects. Materials. 2021; 14: 5360. https://doi.org/10.3390/ma14185360.

[43] Kitahara T, Tateiwa D, Hirai H, Ikuta M, Furuichi T, Bun M, *et al*. rhBMP-2-loaded hydroxyapatite/beta-tricalcium phosphate microsphere/hydrogel composite promotes bone regeneration in a novel rat femoral nonunion model. Frontiers in Bioengineering and Biotechnology. 2024; 12: 1461260. https://doi.org/10.3389/fbioe.2024.1461260.

[44] Cen C, Wang C, Zhang Y, Hu C, Tang L, Liu C, *et al*. Osteoimmunomodulation unveiled: Enhancing bone regeneration with 3D-printed PLLA/β-TCP/CS scaffolds. Colloids and Surfaces. B, Biointerfaces. 2025; 252: 114674. https://doi.org/10.1016/j.colsurfb.2025.114674.

[45] Badwelan M, Alkindi M, Alghamdi O, Saeed WS, Al-Odayni AB, Alrahlah A, *et al*. Poly(δ-valerolactone)/Poly(ethylene-co-vinylalcohol)/β-Tri-calcium Phosphate Composite as Scaffolds: Preparation, Properties, and *In Vitro* Amoxicillin Release. Polymers. 2020; 13: 46. http://doi.org/10.3390/polym13010046.

[46] Chen H, Ji C, Hu H, Hu S, Yue S, Zhao M. Bacterial community response to chronic heavy metal contamination in marine sediments of the East China Sea. Environmental Pollution. 2022; 307: 119280. https://doi.org/10.1016/j.envpol.2022.119280.

Editor's note: The Scientific Editor responsible for this paper was Chris Evans.

Received: 9th April 2025; **Accepted**: 20th June 2025; **Published**: 28th August 2025